Journal Pre-proof

Rational design of visible-light-sensitive Ag-$BiVO_4$ oxides by matching redox potentials of catalyst, dyes, and reactive oxygen species towards more efficient photocatalytic degradation

Andrei Lebedev (Methodology) (Validation) (Formal analysis) (Resources) (Writing - original draft), Franklin Anariba (Conceptualization) (Resources) (Writing - review and editing), Xu Li (Supervision) (Software), Ping Wu (Conceptualization) (Formal analysis) (Investigation) (Writing - review and editing) (Supervision) (Project administration) (Funding acquisition)

PII: S2213-3437(20)30096-8

DOI: https://doi.org/10.1016/j.jece.2020.103748

Reference: JECE 103748

To appear in: *Journal of Environmental Chemical Engineering*

Received Date: 10 September 2019

Revised Date: 13 January 2020

Accepted Date: 3 February 2020

Please cite this article as: Lebedev A, Anariba F, Li X, Wu P, Rational design of visible-light-sensitive Ag-$BiVO_4$ oxides by matching redox potentials of catalyst, dyes, and reactive oxygen species towards more efficient photocatalytic degradation, *Journal of Environmental Chemical Engineering* (2020), doi: https://doi.org/10.1016/j.jece.2020.103748

Rational design of visible-light-sensitive Ag-$BiVO_4$ oxides by matching redox potentials of catalyst, dyes, and reactive oxygen species towards more efficient photocatalytic degradation

Andrei Lebedev[1], Franklin Anariba[1, 2], Xu Li[3], and Ping Wu[1]*

[1]Entropic Interface Group, Engineering Product Development, Singapore University of Technology and Design, Singapore

[2]Materials Surface Group, Science and Math affiliated to Engineering Product Development, Singapore University of Technology and Design, Singapore

[3]A-Star, Institute of Materials Research and Engineering (IMRE), Singapore

*Corresponding author: Ping Wu, E-mail address: wuping@sutd.edu.sg

Highlights

- Ag-$BiVO_4$ is synthesized by photo-deposition method
- Ag-$BiVO_4$ is designed to match with ROS and dyes' redox potentials (rational design)
- Material has been tested under LED towards degradation of cationic and anionic dyes
- Catalyst degrades MB and BG by 91 % and 84 % within 20 min, respectively
- Catalyst degrades AR and MO by 79 % and 65 % within 60 and 120 min, respectively.

Abstract

By employing a rational design approach of matching redox potentials of dye, catalysts, and reactive oxygen species (ROS), Ag-$BiVO_4$ photo-catalysts of 2, 5 and 7 wt% Ag were successfully prepared via sol-gel and UV photo-reduction methods. The as-prepared composites over-perform existing counterparts by exhibiting excellent photocatalytic properties towards degradation of cationic methylene blue (MB, 20 min, 90.9 ± 2.4 %), brilliant green (BG, 20 min, 84.0 ± 2.7 %) and rhodamine B (RhB, 120 min, 90.5 ± 3.3 %) as well as anionic acid red 1 (AR, 60 min, 79.0 ± 2.5 %) and methyl orange (MO, 120 min, 64.9 ± 2.0 %) dyes. Furthermore, based on our novel approach of rational design, the degradation of MB dye was ascribed to photoelectrons from *n*-type $BiVO_4$, while degradation of MO and AR was attributed to photo-holes from *p*-type Ag_2O. Meanwhile, BG and RhB dyes degrade due to photoelectrons and photo-oxidation by ROS, which was confirmed by carrier scavenger experiments. Results indicate that Ag-$BiVO_4$ oxide can be efficiently used for wastewater treatment, solar energy, water splitting, and medicine.

Keywords: photocatalysis, dye degradation, rational design, solar energy, visible light, reactive oxygen species

Introduction

In our previous reports [1, 2] we developed a rational design strategy for predicting the efficiency of dye degradation process based on the mapping of (1) catalysts' energy bands with reactive oxygen species (ROS) redox potentials, (2) ROS redox potentials with molecular orbitals of dyes, and (3) molecular orbitals with energy bands of dyes and

catalysts, respectively. Next, based upon the proposed chemical reactions and positions of ROS redox values vs. valence band (VB)/conduction band (CB) of catalysts in the system, we were able to estimate the relative yield of O_2^-, H_2O_2, and $^{\bullet}OH$ during photocatalytic process. Finally, based upon the estimated relative yield of ROS and HOMO/LUMO positions of pollutants, the role of ROS in the photo-oxidation process was predicted. HOMO and LUMO stand for highest occupied molecular orbital and lowest unoccupied molecular orbital, respectively, and define energy levels in molecules, such as organic dyes.

For our current system of study Ag-$BiVO_4$, relevant redox potentials are shown in Figure 1, where CB of $BiVO_4$ is 0.00 eV [3] and VB is 2.25 eV vs. NHE (from absorbance measurements in Figure 4). CB/VB of Ag nanoparticles (NPs) are 0.69/2.8 eV and Ag_2O are 0.34/2.34 eV vs. NHE, respectively [4]. The redox values of ROS are -0.33, 0.94, 0.32, and 2.33 V vs. NHE for O_2, O_2^-, H_2O_2, and $^{\bullet}OH$, respectively [5, 6]. HOMO/LUMO values of cationic methylene blue (MB) and rhodamine B (RhB) are 0.065/1.77 eV and 0.54/2.78 eV, respectively [7, 8]. HOMO/LUMO values of anionic acid red 1 (AR) and methyl orange (MO) are -0.2/2.14 eV and -0.036/1.644 eV vs. NHE, respectively [9, 10]. Molecular orbital values of brilliant green (BG) were estimated from the literature [11]. $BiVO_4$ and Ag NPs are *n*-type materials, while Ag_2O is a *p*-type material with photoelectrons and photo-holes as predominant charge carriers, respectively. Consequently, electrons are responsible for photocatalytic degradation of cationic dyes (MB, RhB and BG), while photo-holes drive degradation of anionic pollutants (AR and MO).

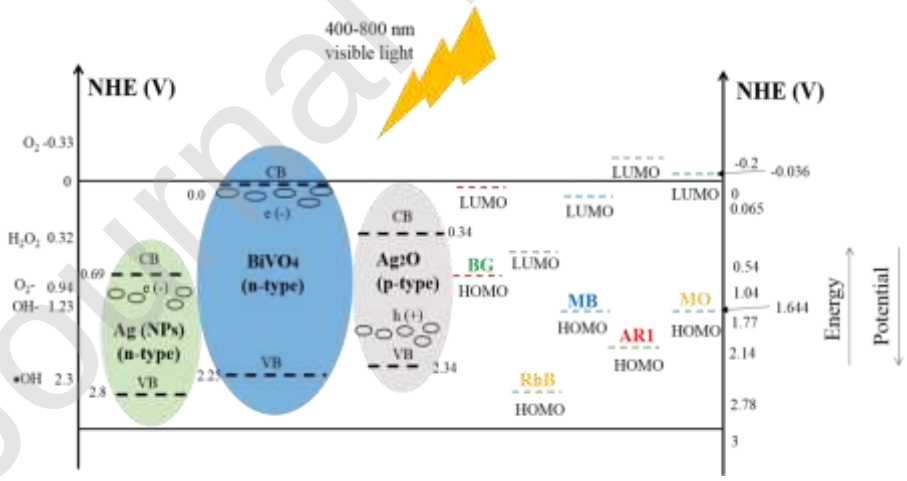

Figure 1: Schematic of relative positions of VB/CB of $BiVO_4$, Ag_2O and Ag NPs and HOMO/LUMO of cationic BG, RhB, MB and anionic AR and MO dyes.

In this work, we extend our rational design approach by mapping Figure 1 to discern between photocatalytic and photo-oxidative degradation pathways. Through a series of radicals, electrons, and holes scavenging experiments and matching strategy of dyes' and

catalysts' energy bands with ROS redox potentials, it was found out that MB, MO and AR dyes degrade due to interaction with photoelectrons and photo-holes, while RhB and BG dyes degrade due to combination of photo-oxidation by ROS and photo-holes. For such a task, we synthesized Ag-$BiVO_4$ by sol-gel and UV photo-reduction methods and carried out a comprehensive dye degradation study under visible light of cationic MB, RhB and BG and anionic AR and MO.

Experimental

2.1 Preparation

Reagents. Bismuth nitrate pentahydrate ($Bi(NO_3)_3 \cdot 5H_2O$, 98%, Sigma-Aldrich) and ammonium metavanadate (H_4NO_3V, 99%, Sigma-Aldrich) were purchased as precursor for bismuth and vanadium sources, respectively. Silver nitrate ($AgNO_3$) was purchased as a source of silver from Sigma-Aldrich. Acetic acid (CH_3COOH, 99%, Alfa Aesar), nitric acid (HNO_3, 70%, Sigma-Aldrich), ethanol (CH_3CH_2OH, 96%, Sigma-Aldrich) and deionized water (DI, 50 KΩ) were used as solvents throughout all experiments. Methylene Blue (dye content ≥ 82%), Brilliant Green (dye content ≥ 95%), Acid Red 1 (dye content 60%), Rhodamine B (dye content ≥ 95%) and Methyl Orange (dye content 85%) were purchased from Sigma-Aldrich.

Pristine $BiVO_4$ and Ag-$BiVO_4$ synthesis. Monoclinic $BiVO_4$ was prepared by following the recipe from our previous work [2]. Ag-$BiVO_4$ with 2 wt%, 5 wt% and 7 wt% loading of Ag were synthesized by photo-deposition method. During preparation, 0.1 g of pristine $BiVO_4$ was dispersed in 1 mL of ethanol and the corresponding amount of $AgNO_3$ was added to obtain 2-7 wt% Ag. The solution was stirred for 180 min, the intensity of UV light was set for 14 mW/cm^2, the distance between vial and the light source was kept for 2 cm. At the last stage of synthesis ethanol was evaporated and Ag-$BiVO_4$ composites were used for further characterization and dye degradation experiments.

2.2. Instrumentation

X-ray diffraction (XRD) experiments were carried out on a Bruker D8 Advance X-ray diffractometer with Cu Kα radiation of 0.154 nm wavelength to evaluate powder's composition and phase. The scanning angle was set from 25℃ to 60℃. UV-Vis absorbance spectra were recorded and monitored by using a PG Instruments TIIO+ UV-Vis spectrophotometer. Surface morphology of samples was examined by scanning electron microscopy (SEM) JEOL JSM-7600F. Fourier-transform infrared spectroscopy (FTIR)

spectra was carried out from 400 cm^{-1} to 1200 cm^{-1} by a Vertex 70 (Bruker). Chemical composition and phase structure was recorded by X-ray photoelectron spectroscopy (XPS) with a Thermo Fischer Scientific Theta Probe system. Annealing of the sample was performed in a box furnace (Anhui Haibei 1100 model). Photoluminescence (PL) tests with 254 and 365 nm excitation wavelength, was carried out by a QE Pro spectrofluorometer (Ocean Optics, USA). A Prizmatix Ultra High Power LED lamp (48 W) was used as a light source during dye degradation experiments. The light intensity was monitored by an Optical Power Meter PM100D from Thorlabs. Zeta potential was measured by NanoBrook Omni device in PALS mode.

2.3 Photocatalyic tests

The photocatalytic tests were conducted for MB, BG, RhB, AR and MO dyes in aqueous solution under visible light irradiation of 100 mW/cm^2. During a typical experiment 15 mg of catalyst were dispersed in 15 mL of water (1 g L^{-1} concentration) and sonicated for 1 hour. After that, the solution was mixed with dye with the concentration 1 g L^{-1} and kept in dark for 30 min to achieve adsorption-desorption equilibrium. The same concentration was used for all dyes. Next, the suspension was transferred into 1.5 mL centrifuge tubes and the LED lamp was switched on. For each measurement, 1 mL of the solution was collected, centrifuged for 5 min, and transferred to the cuvette for UV-Vis absorption experiments.

Results and Discussions

3.1 Structural Characterization of Catalyst

Figure 2 shows the X-ray diffraction (XRD) patterns for pristine $BiVO_4$ and Ag-$BiVO_4$ with different Ag loadings. It can be seen that material possess monoclinic scheelite structure (JCPDS Card no. 14-0688). No peaks from other phases were detected, indicating high purity of the synthesized composite. The major (121) peak exhibits shift to the lower angle from 28.698° for pristine $BiVO_4$ to 28.685°, 28.659° and 28.631° for 2, 5, and 7 wt% Ag, respectively. Facet (040) also demonstrates lower angle shift from 30.461° for pristine $BiVO_4$ to 30.434°, 30.408° and 30.381° for 2, 5, and 7 wt% Ag, respectively. Lower angle shift can be attributed to either (1) cationic or (2) anionic doping as we showed earlier [2]. Cationic doping is consistent with the fact that Bi^{+3} ions (100 pm) can be substituted by slightly larger Ag^{+} ions (110 pm). Vanadium (V^{+5}) ions are less likely to be replaced due to

smaller size (49.5 pm) [12]. Due to the low Ag presence, no corresponding XRD peaks were detected.

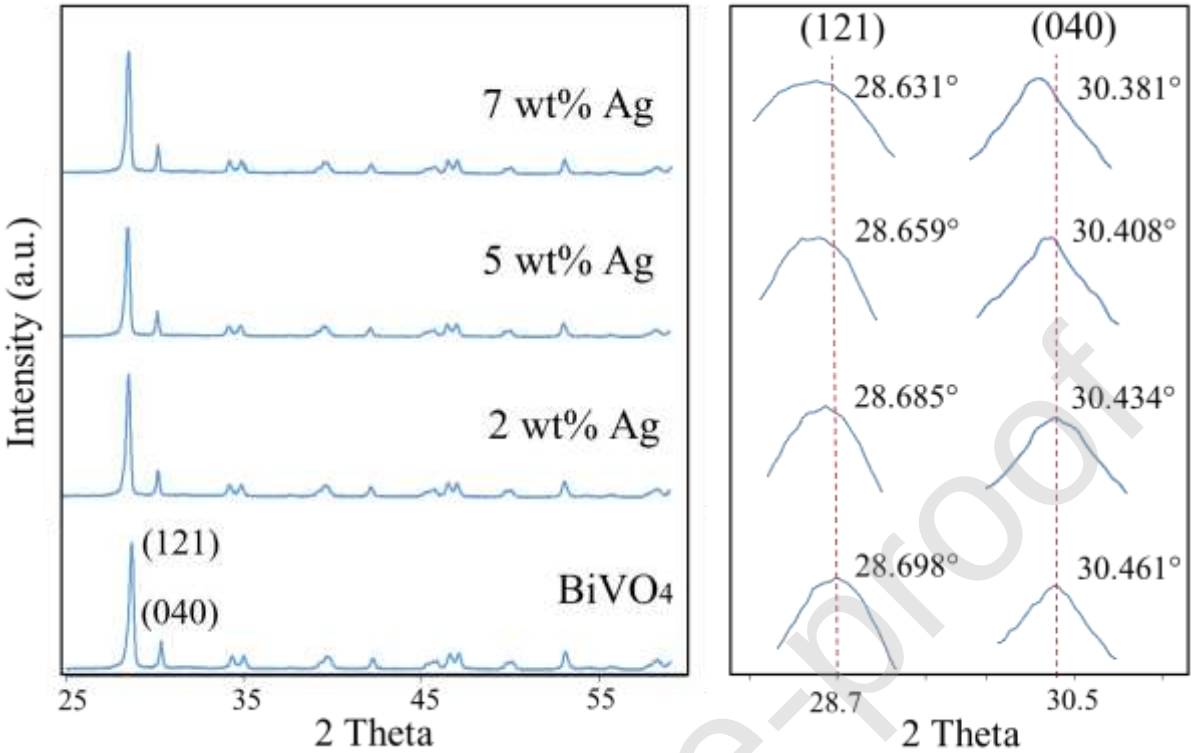

Figure 2: Left panel: XRD profiles for pristine $BiVO_4$ and Ag-$BiVO_4$ with 2, 5 and 7 wt% Ag loading. Right panel displays (121) and (040) peaks associated with a shift to lower angles.

The Fourier-transform infrared spectroscopy (FTIR) at 400-1200 cm^{-1} range was applied to characterize chemical bonds of $BiVO_4$ and Ag-$BiVO_4$ catalysts as shown in Figure S1 in the Supplementary Information (SI). No Ag-related bands in bulk were observed indicating the absence of chemical bonding between Ag and $BiVO_4$. The intense band at 474 cm^{-1} is ascribed to symmetric bending of VO_4^{3-} [13]. The weak and intense absorption bands at 554 cm^{-1} and 606 cm^{-1} are the signs of bending vibration of Bi-O bonds, respectively [14]. Bands at 661 cm^{-1} and 811 cm^{-1} are associated with asymmetric and symmetric stretching of VO_4^{3-}, respectively [13, 14]. In summary, the FTIR spectra confirm the presence of monoclinic $BiVO_4$.

Figure 3 shows high-resolution X-ray photoelectron spectrum (XPS) to evaluate chemical states of C, Bi, V, O and Ag elements of 7 wt% Ag-$BiVO_4$. The XPS spectra of C 1s is displayed in Figure 3 (panel A) and suggests the presence of C=O and C-OH bonds (290.1 eV and 287.4 eV, respectively) [15]. The Bi 4f peaks (panel B) at 158.9 eV and 164.2 eV represent metallic Bi^0, while peaks at 164.1 eV and 169.4 eV ascribed to Bi^{+3} chemical

state [14, 16]. The O 1s and V 2p peaks are overlapped and shown in Figure 3 (panel C). The V 2p peaks at lowest binding energies of 516.5 eV and 524.1 ascribed to metallic V^0, while doublets at 521.8 eV and 529.4 eV attributed to V^{+5} state. The largest O1 s peak at 529.7 ascribed to O^{2-} anions (Bi-O bonds) [14]. The O 1s peaks at 530.8 eV and 534.6 eV can be assigned to V-O bond and surface adsorbed oxygen species, respectively [14, 16]. Panel D confirms the presence of metallic Ag (368.3 eV and 374.3 eV) and Ag_2O (371.3 eV and 377.4 eV). Figure S2 in the SI compares chemical states of Ag for pristine monoclinic $BiVO_4$ and Ag-$BiVO_4$ catalysts. Table S2 in SI shows the atomic % of metallic Ag^0 and Ag^+ in 2 wt%, 5 wt% and 7 wt% Ag-$BiVO_4$, respectively. With larger Ag loading the amount of Ag^0 gradually increases from 2.55 at. % to 6.56 at. %, while Ag^+ increases slower (2.19-2.91 at. %). The total presence of Ag in both chemical states increases from 4.74 atomic % for 2 wt% Ag to 6.37 atomic % and 9.47 atomic % for 5 wt% Ag and 7 wt% Ag, respectively.

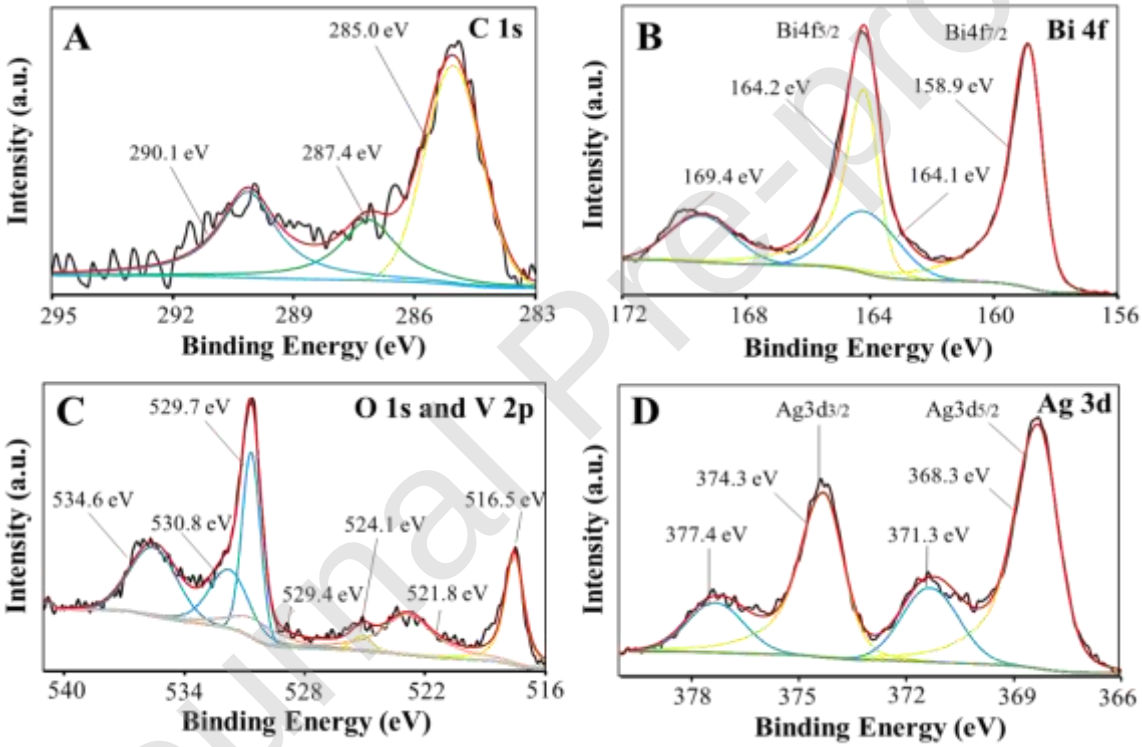

Figure 3: XPS spectra of 7 wt% Ag-$BiVO_4$ for A) C 1s; B) Bi 4f; C) O 1s and V 2p and D) Ag 3d.

The optical properties of samples were investigated by measuring the absorbance as the function of the wavelength, see Figure 4. The corresponding band gap was calculated from a plot depicting $(\alpha h\nu)^2$ versus $(h\nu)$ and shown on the inset of Figure 4. Absorption edges were found to be 551.11 nm, 556.05 nm, 570.73 nm and 573.48 nm for $BiVO_4$, 2 wt% Ag, 5 wt% Ag and 7 wt% Ag, respectively. It can be seen that the absorbance spectra of Ag-$BiVO_4$ are red-shifted in comparison with pristine monoclinic $BiVO_4$, which can be explained by

surface plasmon resonance (SPR) effects. As a result, incorporation of Ag reduces the band gap: for example, for 2 wt% Ag loading the band gap slightly drops in comparison with pristine $BiVO_4$, 2.23 eV vs. 2.25 eV, respectively. Higher Ag loading leads to enhanced absorption capacity of visible light with the band gaps of 2.17 and 2.16 eV for 5 wt% and 7 wt% Ag, respectively.

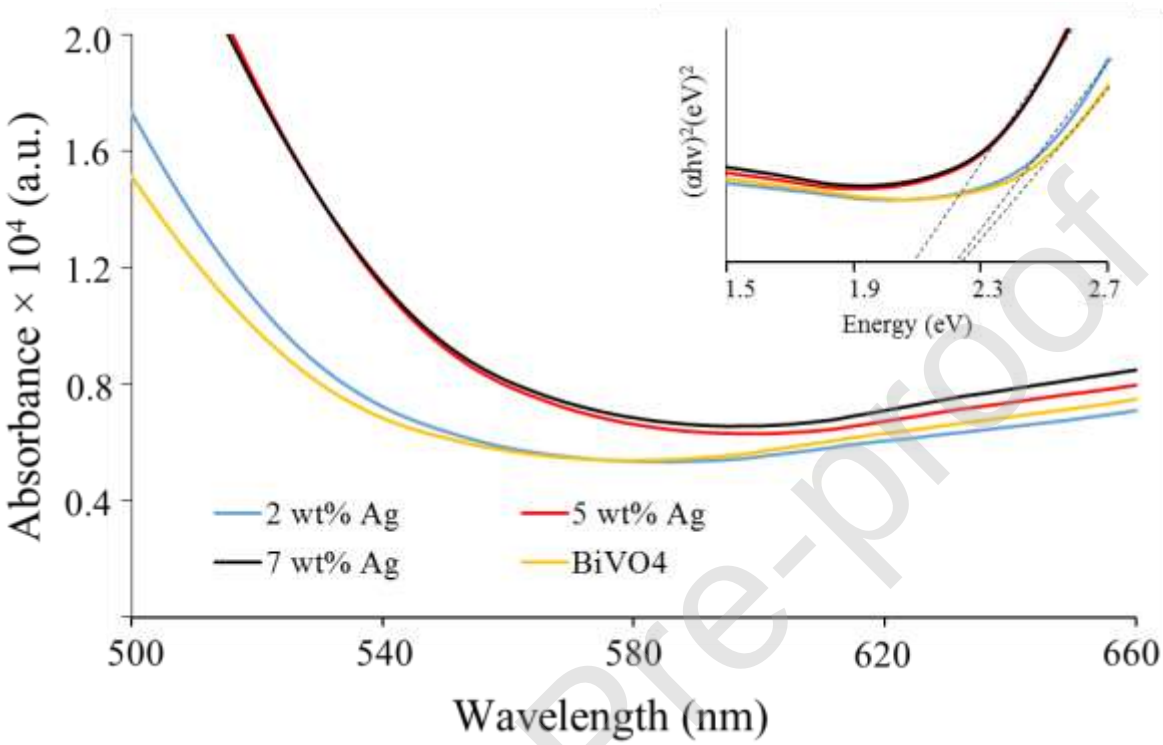

Figure 4: UV-Vis absorbance spectroscopy of pristine monoclinic $BiVO_4$ and Ag-$BiVO_4$ composites. Inset of the plot shows band gap values based on extrapolation of the linear segment of $(\alpha hv)^2$ versus hv for pristine $BiVO_4$ and Ag-$BiVO_4$.

The room temperature photoluminescence (PL) technique (λ_e = 254 nm) was employed to investigate the electron-hole recombination rate in the as-prepared samples (Figure S3 in SI), where the less intense PL signal manifests enhanced charge carrier separation efficiency [17]. The most intense UV-light-induced peak is located at 537 nm and attributed to pristine $BiVO_4$. The peak corresponds to electron-hole recombination where holes formed in the O 2p band and electrons are in the V 3d band [18]. The intensity of PL peak drastically drops when Ag introduced. The weakest PL signal was recorded from 2 wt% Ag, indicating major inhibition of electron-hole recombination. Furthermore, the red-shift from 537 nm for $BiVO_4$ to 516-520 nm for Ag-$BiVO_4$ composites demonstrates the interaction among metallic Ag, Ag_2O and $BiVO_4$ [14, 19]. Therefore, incorporation of Ag leads to suppressed recombination rate of charge carriers.

Representative SEM images of the as-synthesized pristine $BiVO_4$ (panels A and B)

and 7 wt% Ag-$BiVO_4$ (panels C and D) are shown in Figure 5. $BiVO_4$ particles has microsphere morphology with 1-2 μm diameter. When Ag is added there is no significant morphological change observed. Based on SEM results, it can be concluded that the UV photo-reduction synthesis method does not affect the morphology of Ag-$BiVO_4$ catalyst.

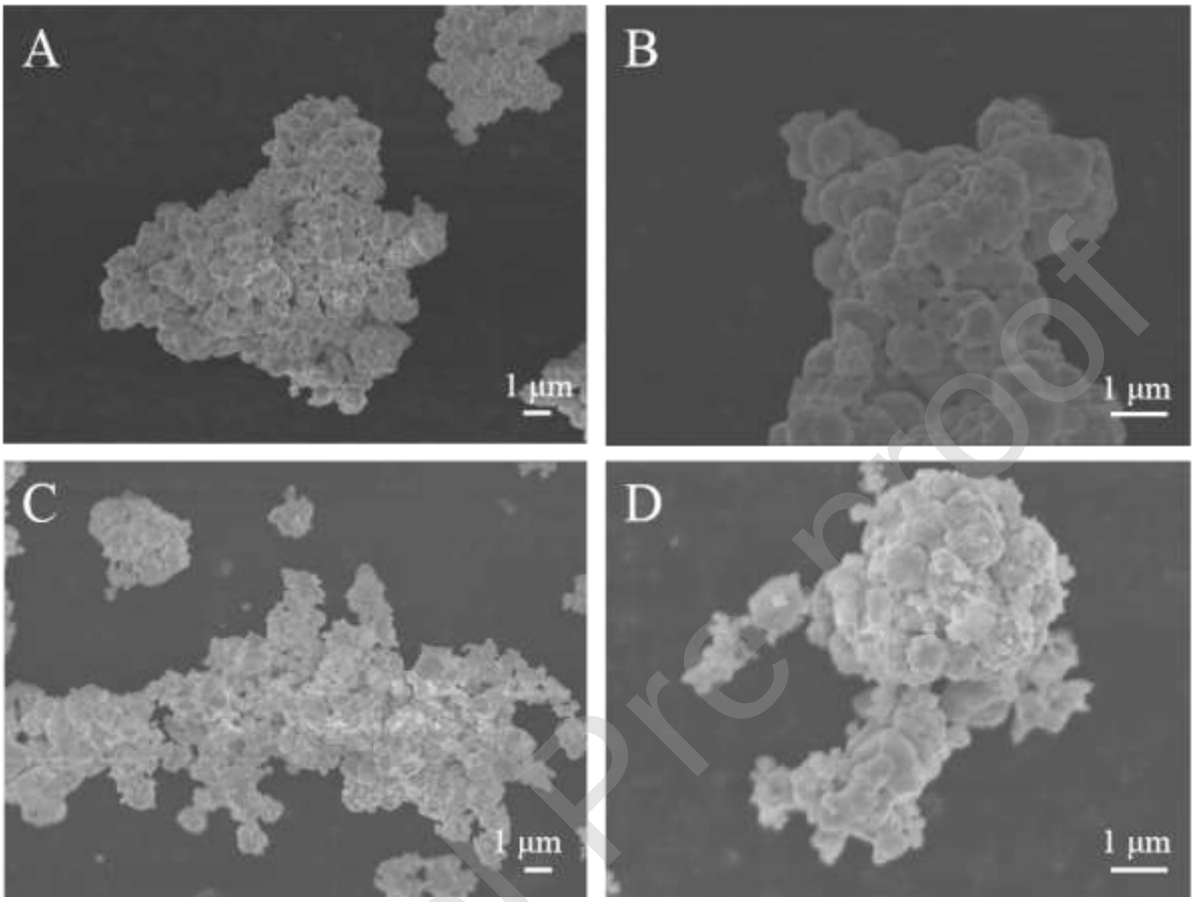

Figure 5: SEM representative images of pristine monoclinic $BiVO_4$ (panels A and B) and 7 wt% Ag-$BiVO_4$ (panels C and D).

3.2 Photocatalytic degradation of anionic acid red 1 (AR) and methyl orange (MO) dyes

The photocatalytic activity of as-prepared composites was evaluated for 60 min and 120 min under LED light by degradation of anionic AR and MO dyes, respectively. Degradation kinetics was routinely monitored by UV-Vis spectroscopy of the main characteristic bands at 517 nm for AR and at 465 nm for MO, with results shown in Figure 6. Panels A and C depict the change in degradation rate, where C_0 is the concentration of pollutant after adsorption-desorption equilibrium and C is the concentration at the certain irradiation time. Panels B and D show the Langmuir-Hinshelwood model by plotting first-order reaction curves. Blank experiments (photolysis) were carried out to confirm the major

role of Ag-$BiVO_4$ catalyst in the degradation process. Further information of absorption bands of 7 wt% Ag-$BiVO_4$ are shown in Figure S4, panels A and B in SI.

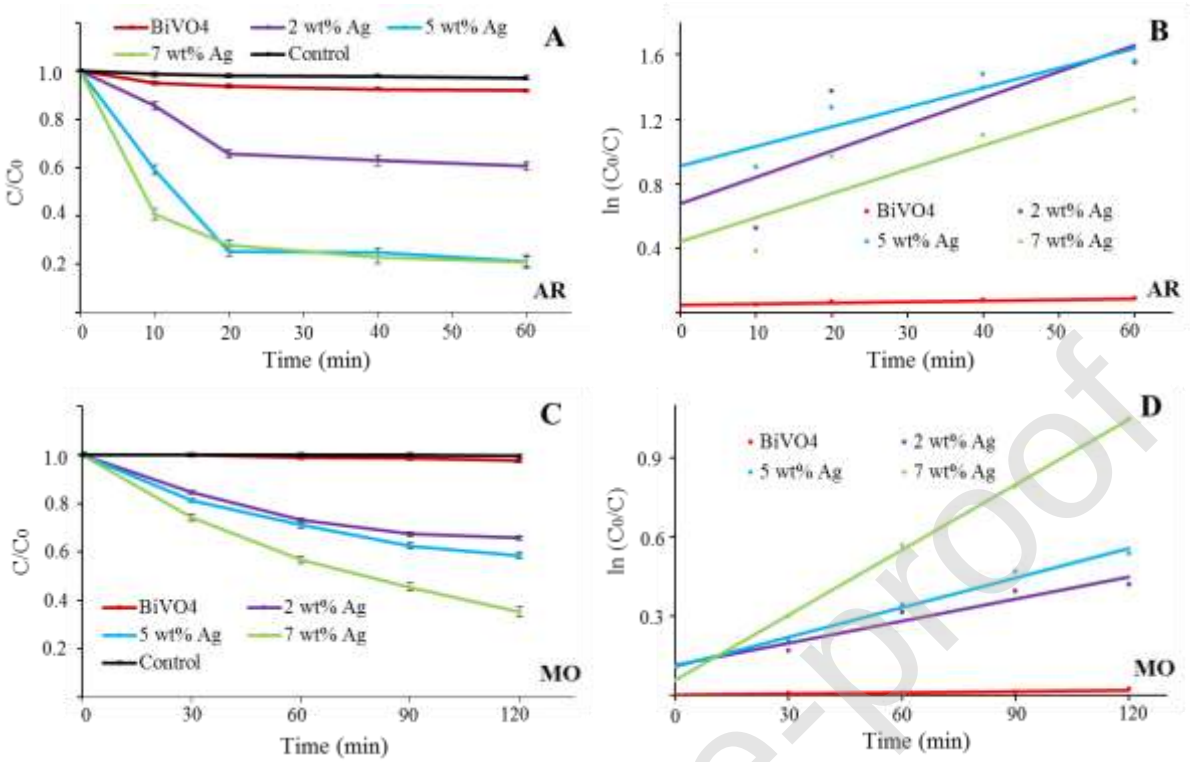

Figure 6: Normalized photocatalytic degradation by pristine $BiVO_4$ and Ag-$BiVO_4$ (2, 5 and 7 wt% Ag) for A. AR and C. MO dyes. First-order kinetic plots for B) AR and D) MO dyes. Error bars based on the standard deviation for n = 3 measurements.

Visible-light degradation of AR by pristine $BiVO_4$ is negligible (8.1 ± 0.7 %) and comparable to photolysis results. Once Ag is introduced on the $BiVO_4$ surface, degradation rate increases to 39.3 ± 1.9 % and 78.8 ± 2.5 % for 2 wt% Ag and 5 wt% Ag, respectively, and reaches a maximum value of 79.0 ± 2.5 % for 7 wt% Ag. Interestingly, no significant change was observed in removal rate between 5 wt% Ag and 7 wt% Ag, which can be attributed to minor *p*-type Ag_2O content difference on the $BiVO_4$ surface (from Table S2, 0.41 atomic % Ag_2O difference between 5 wt% Ag and 7 wt% Ag, respectively). The increase in AR removal rate from 8.1 ± 0.7 % for pristine $BiVO_4$ to 39.3 ± 1.9 % for 2 wt% Ag can also be explained by major contribution of 2.19 atomic % of *p*-type Ag_2O. On the other hand, the drastic difference in AR degradation between 2 wt% Ag and 7 wt% Ag cannot be ascribed to the effect of Ag_2O only (0.72 atomic % Ag_2O increase between 2 wt% Ag and 7 wt% Ag). Here, rapid AR degradation was likely induced by the formation of $^{\bullet}OH$ radicals from interaction of photo-generated charge carriers, electrons from metallic Ag and holes from Ag_2O, respectively, with water molecules [20].

Figure 6, panels C and D, shows degradation of anionic MO dye in the presence of photocatalyst under visible light. After 120 min a notable intensity decrease was observed at 465 nm, indicating continuous process of intermediates formation as was previously described here [21, 22]. First, one of the benzene rings was replaced with OH^- group due to attack of $^{\bullet}OH$ radicals. Second, the breakage of N-C bond in dimethylamino group causes the replacement of methyl group with protons. Finally, the breakage of the main azo double bond -N=N- (color-bearing group) due to ROS attack leads to formation of inorganic sub-products. Evidently, the highest degradation rate was achieved with 7 wt% Ag (64.9 ± 2.0 %), while with 5 wt% Ag and 2 wt% Ag the removal rate dropped to 41.5 ± 1.6 % and 34.2 ± 1.3 %, respectively. Similarly to anionic AR, the difference in degradation rate between pristine $BiVO_4$ and 2 wt% Ag-$BiVO_4$ can be attributed to *p*-type Ag_2O (2.19 atomic % from Table S2), while the difference in removal rate between 2 wt% Ag and 7 wt% Ag-$BiVO_4$ cannot be explained by Ag_2O contribution only (0.72 atomic % Ag_2O increase between 2 wt% and 7 wt%). The latter change in MO removal rate is possibly attained to the detrimental effect of ROS, like $^{\bullet}OH$, H_2O_2 and O_2^- radicals.

Degradation kinetics of AR and MO dyes was routinely analysed by Langmuir-Hinshelwood model. The first-order model was applied:

$$\ln(C_0/C) = kt, \quad (1)$$

where C_0/C is the ratio of concentration of dye solution at adsorption-desorption equilibrium, and *k* is the first order constant (min^{-1}). Based on first-order model, *k* values were collected and analysed, where largest *k* implies better dye degradation properties. Both total degradation, % and *k* constant values for anionic dyes are summarized in Table 1.

Table 1. Total degradation (%) and k constant values (min^{-1}) for AR and MO dyes, respectively.

	AR (60 min)		MO (120 min)	
	Total degradation, %	*k* constant (min^{-1})	Total degradation, %	*k* constant (min^{-1})
$BiVO_4$	8.1 ± 0.7[a]	0.0012[b]	-[c]	-
2 wt% Ag	39.3 ± 1.9	0.0198	34.2 ± 1.3	0.0036
5 wt% Ag	78.8 ± 2.5	0.0239	41.5 ± 1.6	0.0044
7 wt% Ag	79.0 ± 2.5	0.0223	64.9 ± 2.0	0.0086

[a] Average and standard deviation values are based on n = 3 measurements. [b] *k* value reported is the highest rate constant obtained, [c] dye degradation value is below 5 %.

3.3 Photocatalytic degradation of cationic methylene blue (MB), brilliant green (BG) and rhodamine B (RhB) dyes

Photocatalytic degradation of cationic MB, BG and RhB was monitored under LED irradiation and recorded by using UV-Vis spectroscopy. Decolorization of MB and BG was evaluated for 20 min with measurements taken every 5 min, while removal rate of RhB was studied for 120 min with measurements taken every 30 min. The results are shown in Figure 7.

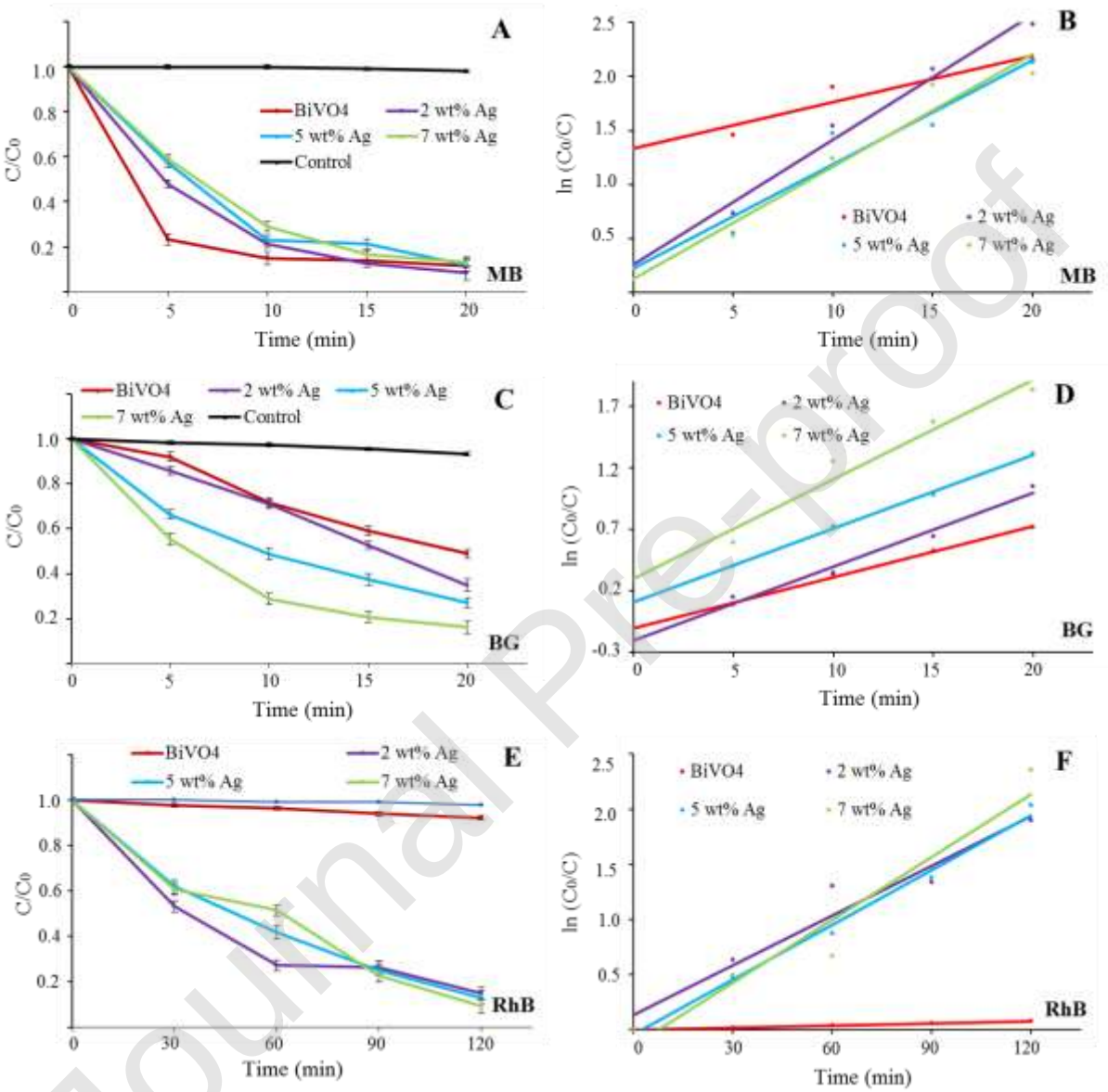

Figure 7: Normalized photocatalytic degradation by pristine $BiVO_4$ and Ag-$BiVO_4$ (2, 5 and 7 wt% Ag) for A) MB, C) BG and E) RhB dyes. First-order kinetic plots for B) MB, D) BG and F) RhB dyes. Error bars based on the standard deviation for n = 3 measurements.

MB degradation is shown in panels A and B. Under visible light, decomposition of MB is largely independent from the Ag presence with best result ascribed to 2 wt% Ag and 7 wt% Ag (91.7 ± 3.1 % and 90.9 ± 2.4, respectively). The results can be explained by direct match of CB from *n*-type $BiVO_4$ with LUMO level of MB, where *p*-type Ag_2O and metallic

Ag do not participate in the photocatalytic reaction (we elaborate more in "Proposed mechanism of dye degradation" section). MB exhibits two main absorption peaks at 668 nm and 615 nm. The major peak at 668 nm is characteristics of conjugation system between the two dimethylamine substituted aromatic rings through the nitrogen and sulfur, while the minor peak at 615 nm is attributed to dye dimmer [23]. Both peaks retard gradually with slightly faster kinetics ascribed to the 615 nm peak, see Figure S5, panel A in the SI.

Degradation of BG is shown in panels C and D. Cationic BG degrades mainly due to contribution of *n*-type $BiVO_4$ (51.1 ± 2.0 %). With Ag presence degradation rate increases to 65.2 ± 2.7 %, 73.0 ± 2.3 % and 84.0 ± 2.7 % for 2, 5, and 7 wt% Ag, respectively, which can be explained by self-sensitization mechanism and photo-oxidation by ROS (more details in "Proposed mechanism of dye degradation" section). No hypsochromic shift of main absorption band at 619 nm was observed, indicating BG chromophore destruction, as shown in Figure S5, panel B in the SI [24].

Degradation of RhB was investigated for 120 min and shown in panels E and F. Pristine $BiVO_4$ is not sufficient to induce breakage of the dye given a decomposition rate of 12.1 ± 0.7. Higher presence of Ag leads to enhanced degradation rate with 85.5 ± 2.8 %, 86.9 ± 3.0 % and 90.5 ± 3.3 %, for 2, 5 and 7 wt% Ag, respectively. The main absorption peak is located at 535 nm wavelength, as shown in Figure S5, panel C in the SI, indicating the $n \rightarrow \pi^*$ transition of C=N and C=O groups [25]. No hypsochromic peak shift was observed, suggesting degradation pathway via (1) chromophore cleavage, (2) hydroxylation, (3) aromatic ring opening and, finally (4) mineralization [25]. The major role in RhB degradation is attributed to *n*-type metallic Ag NPs on the surface and photo-oxidation by ROS. Although, the CB level of Ag is slightly more positive than LUMO level of RhB, breakage of dye molecule can be accomplished by self-sensitization mechanism. Both total degradation, % and *k* constant values for cationic dyes are summarized in Table 2.

Table 2. Total degradation (%) and k constant values (min^{-1}) for MB, BG and RhB dyes, respectively.

	MB (20 min)		**BG (20 min)**		**RhB (120 min)**	
	Total degradation, %	*k* constant (min^{-1})	Total degradation, %	*k* constant (min^{-1})	Total degradation, %	*k* constant (min^{-1})
$BiVO_4$	88.4 ± 2.4[a]	0.0964[b]	51.1 ± 2.0	0.0373	12.1 ± 0.7	0.0006
2 wt% Ag	91.7 ± 3.1	0.1259	65.2 ± 2.7	0.0519	85.5 ± 2.8	0.015
5 wt% Ag	88.1 ± 2.7	0.1051	73.0 ± 2.3	0.0640	86.9 ± 3.0	0.0165
7 wt% Ag	90.9 ± 2.4	0.1091	84.0 ± 2.7	0.0928	90.5 ± 3.3	0.0189

[a] Average and standard deviation values are based on n = 3 measurements. [b] *k* value reported is the highest rate constant obtained.

3.4 Radical, electron, and hole scavenger tests

Species involved in the process of dye degradation were further identified by adding *p*-benzoquinone (BQ), EDTA and isopropanol (IP) to the analyte solutions as scavengers to capture electrons, holes and •OH radicals, respectively [26]. Results are shown in Figure 8.

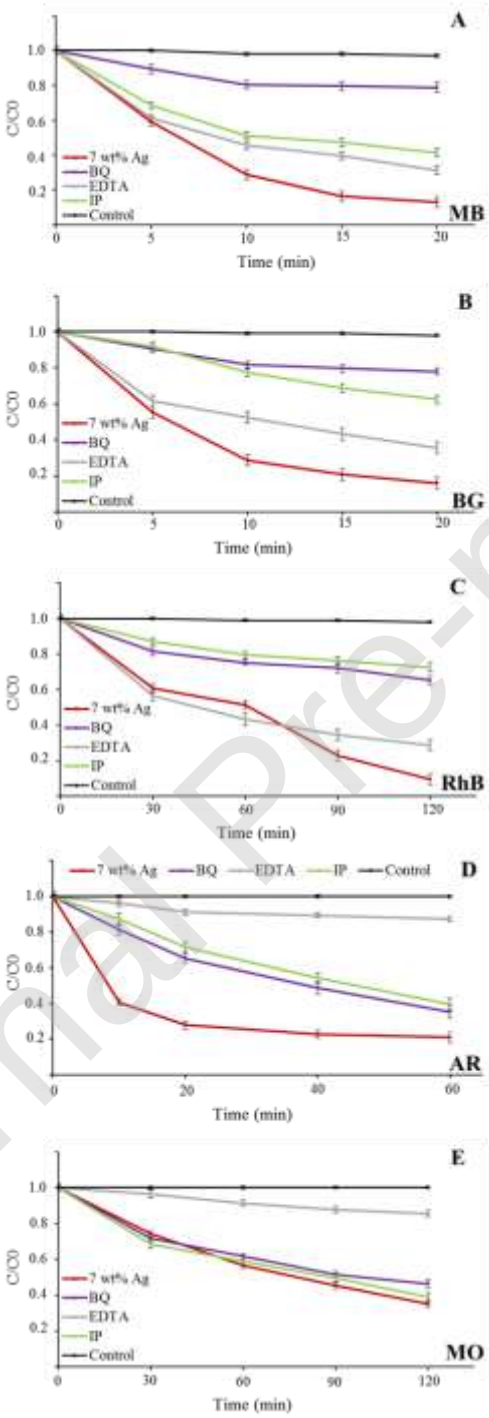

Figure 8: Normalized photocatalytic degradation curves with 7 wt% Ag-$BiVO_4$ in the presence of scavengers (BQ, EDTA, IP) for A) MB, B) BG, C) RhB, D) AR and E) MO. Error bars based on the standard deviation for n=3 measurements.

Anionic AR and MO dyes degrade due to contribution of photo-holes, as shown by degradation rates of 12.8 ± 1.5 % and 14.6 ± 1.8 %, respectively. Cationic MB decomposes at a rate of 21.2 ± 3.0 % due to photoelectrons with very minor role of photo-holes and $^{\bullet}OH$ radicals. Decomposition of cationic BG and RhB is governed by photoelectrons and $^{\bullet}OH$ radicals, with decomposition rates of 22.1 ± 1.8 % and 27.6 ± 2.3% for BG and 24.7 ± 2.3 % and 27.5 ± 2.4 % for RhB, respectively.

3.5 Proposed mechanism of dye degradation

The efficiency of dye degradation depends upon many parameters: (1) band gap of the catalysts, (2) light intensity and generated number of charge carriers, (3) efficiency of charge carriers (electron-hole pairs) and corresponding recombination rate, (4) amount and type of generated ROS, (5) morphology, (6) structure of dye molecule, and (7) self-sensitization mechanism, etc. In general, photo-degradation of dyes occurs due to photocatalytic attack of electron-holes after transfer and adsorption of dye molecules on the catalyst's surface. Consequently, ROS (O_2^-, H_2O_2, and $^{\bullet}OH$) are produced, from the reaction of charge carriers with water molecules, known as photo-oxidation, and also participate in oxidation of pollutants.

Degradation of cationic MB is driven by photoelectrons from n-type $BiVO_4$. As the CB level of $BiVO_4$ is less positive than LUMO level of MB (0.00 eV vs. 0.065 eV), electrons can freely flow causing rapid degradation within 20 min. Ag NPs as another *n*-type material have minor influence on degradation of MB due to a mismatch of their CB and LUMO levels which is in line with our experimental results from Table 2. Decomposition of cationic BG and RhB follows similar principles with direct electrons transition from CB of $BiVO_4$ or Ag NPs to LUMO level of BG and RhB. Unlike MB, BG and RhB pollutants exhibit more efficient degradation in the presence of Ag, which can be explained by (1) *n*-type Ag NPs and further self-sensitization mechanism [27] and (2) the influence of ROS, which we discuss further (from Figure 8 both dyes degrade due to influence of photoelectrons and $^{\bullet}OH$ radicals). Degradation of anionic AR and MO exclusively depends upon surface Ag, which is attributed to *p*-type Ag_2O. From Figure 1 it can be observed that VB level of Ag_2O is more positive than HOMO of both AR and MO, manifesting the major role of photo-holes in the degradation process, which is confirmed by scavenging tests from Figure 8.

From the above explanation, degradation mechanism of cationic BG and RhB is still unclear and role of ROS need to be discussed further. It can be approached by photo-oxidation mechanism and the formation of ROS from *n*-type Ag NPs. Here, we propose a

sequence of chemical reactions, from most negative to most positive vs. NHE, excluding photolysis as all the dyes are stable under LED light. VB/CB values of catalysts, HOMO/LUMO of dyes and redox values of ROS are shown in Figure 1.

$O_2 + e^- \rightarrow O_2^-$ (ionization of O_2) (2)

The reduction potential of this reaction is -0.33 eV, which is far from CB/VB values of catalysts as well as HOMO/LUMO values of dyes. Thus, we can exclude this reaction from further discussion.

$H_2O_2 + H^+ \leftarrow H_2O + h^+ + {}^{\bullet}OH$ (3)

The reduction potential of reaction is 0.32 eV (production of H_2O_2). Therefore, holes from VB of *p*-type Ag_2O (2.34 eV) can participate in the reaction.

$H_2O_2 + H^+ + e^- \rightarrow H_2O + {}^{\bullet}OH$ (4)

The reaction of $^{\bullet}OH$ production from H_2O_2 has the reduction potential of 2.3 eV. Electrons from CB of both Ag NPs and $BiVO_4$ can participate in the reaction. However, the CB level of Ag NPs is more positive than of $BiVO_4$. As a result, electrons from CB of Ag NPs have to travel shorter distance, yielding larger amount of $^{\bullet}OH$.

$O_2^- + 2\,H^+ \leftarrow H_2O_2 + h^+$ (5)

The reduction potential of production of O_2^- by oxidation of H_2O_2 is 0.94 eV. Therefore, holes from VB of *p*-type Ag_2O can participate in the reaction.

$O_2^- + 2\,H^+ + e^- \rightarrow H_2O_2$ (6)

The reduction potential of H_2O_2 production is 0.32 eV. However, only electrons from CB of $BiVO_4$ can participate in this reaction as CB of Ag NPs is more positive, making their electrons inaccessible for the above reaction.

From the proposed sequence of chemical reactions, it becomes clear that electrons from *n*-type Ag NPs can yield large number of $^{\bullet}OH$ radicals (reaction (4). Additionally, $^{\bullet}OH$ radicals participate in reaction with holes from VB of Ag_2O to produce H_2O_2 (reaction (3). Based on matching of ROS redox values with HOMO/LUMO of BG and RhB, it can be concluded, that RhB and BG are more likely to be degraded due to attack of $^{\bullet}OH$ (within the HOMO/LUMO range of RhB) and H_2O_2 radicals (within the HOMO/LUMO range of BG), respectively. The proposed mechanism finds support in the Zeta potential values shown in SI,

whereby MB is degraded by photoelectrons on the surface stabilized by a positive potential in the double layer, presumably induced by the cationic dye molecules. Similarly, MO and AR are degraded by photoholes on the surface, stabilized by a negative potential in the double layer induced by the anionic dye molecules. Finally, BG and RhB are degraded by photo-oxidation by radical oxygen species, such as $^{*}OH$ an H_2O_2, whose precursors are HO^- and O_2^-, as displayed by the negative Zeta potential value. Thus, degradation of BG and RhB has partially photo-oxidation nature, while MB, AR and MO pollutants undergo pure photocatalytic degradation, which was confirmed by scavenging experiments and the energy mapping approach.

Summary

In this work we designed the monoclinic visible-light-sensitive Ag-$BiVO_4$ catalyst by using the UV photo-reduction method and tested its photocatalyst properties on several pollutants. By employing a combination of (1) strategy where photo-catalysts and dye molecule energy bands match with ROS reduction potentials and (2) charge carrier trapping experiments, we were able to predict and identify the major degradation pathway for each pollutant tested. Thus, cationic MB degrades due to mobile photoelectrons from *n*-type $BiVO_4$, while anionic AR and MO break down due to photo-holes from *p*-type Ag_2O. Cationic RhB and BG undergo the combination of photocatalytic degradation from both *n*-type $BiVO_4$ and Ag NPs and photo-oxidation by $^{\bullet}OH$ and H_2O_2 radicals, respectively. Furthermore, the synthesized composites were able to degrade MB and RhB dyes in 20 min and 120 min, respectively, which over-performs previous materials [14, 28-31], and other pollutants, such as BG (in 20 min), AR (in 60 min) and MO (in 120 min), which have not been previously tested with Ag-$BiVO_4$. The present work suggests that Ag-$BiVO_4$ materials is efficient agent for wastewater treatment, with other potential applications in the fields of solar energy, water splitting and medicine.

Mr. Andrei Lebedev: methodology, validation, formal analysis, resources, writing – original draft.

Dr. Franklin Anariba: conceptualization, resources, writing review & editing.

Prof. Xu Li: supervision, software

Prof. Ping Wu: conceptualization, formal analysis, investigation, writing review & editing, supervision, project administration, funding acquisition

Declaration of interests

Mr. Andrei Lebedev

Dr. Franklin Anariba

Prof. Li Xu

Prof. Ping Wu

Acknowledgements

This work was partially supported by the National Research Foundation, Prime Minister's Office, Singapore, under its Marine Science Research & Development Programme (Award Number MSRDP-P28) and partially sponsored by the MOE Academic Research Fund (AcRF) Tier 2 - MOE2018-T2-1-163 (Singapore). The MIT-SUTD International Design Centre (IDC) is acknowledged for instrument support.

Supplemental Information

Further information on bismuth-based photocatalysts (Table S1), FTIR absorbance spectrum for pristine and 2, 5, 7 wt% Ag-$BiVO_4$ (Figure S1), atomic % and XPS spectrum of Ag and Ag_2O in Ag-$BiVO_4$ oxides (Table S2 and Figure S2, respectively), PL studies (Figure S3), characteristic absorption bands of anionic and cationic dyes of 7 wt% Ag-$BiVO_4$ (Figures S4 and S5, respectively), antibacterial studies of pristine $BiVO_4$ and Ag-$BiVO_4$ catalysts against *E. coli* (survived colonies, Figures S6-S8), zeta potential studies is shown in the Supplemental Information.

Literature

1. Lebedev, A., et al., *Ag/Ag2O/BiNbO4 structure for simultaneous photocatalytic degradation of mixed cationic and anionic dyes.* Solar Energy, 2019. **178**: p. 257-267.
2. Lebedev, A., et al., *Design and fabrication of BiV(O, N)4 p-n homojunction solid solutions for enhanced methylene blue degradation via LED light irradiation.* Solar Energy, 2018. **160**: p. 298-302.
3. Lin, F., et al., *Low-cost dual cocatalysts BiVO4 for highly efficient visible photocatalytic oxidation.* RSC Advances, 2017. **7**(25): p. 15053-15059.
4. Ding, K., et al., *Comparative density functional theory study on the electronic and optical properties of BiMO4 (M = V, Nb, Ta).* Journal of Materials Chemistry A, 2014. **2**(22): p. 8294-8303.
5. Krumova, K. and G. Cosa, *Chapter 1 Overview of Reactive Oxygen Species*, in *Singlet Oxygen: Applications in Biosciences and Nanosciences, Volume 1*. 2016, The Royal Society of Chemistry. p. 1-21.
6. Sahana, M.B., et al., *Quantum confinement effects and band gap engineering of SnO2*

nanocrystals in a MgO matrix. Acta Materialia, 2012. **60**(3): p. 1072-1078.
7. Apostolova, N., et al., *Ceria nanoparticles with rhodamine B as a powerful theranostic agent against intracellular oxidative stress.* RSC Advances, 2015. **5**(97): p. 79423-79432.
8. Ksenzhek, O.S., S.A. Petrova, and M.V. Kolodyazhny, *Electrochemical properties of some redox indicators.* Bioelectrochemistry and Bioenergetics, 1977. **4**(4): p. 346-357.
9. Costa, M.C., et al., *Effect of dye structure and redox mediators on anaerobic azo and anthraquinone dye reduction.* Química Nova, 2012. **35**: p. 482-486.
10. Trandafilović, L.V., et al., *Enhanced photocatalytic degradation of methylene blue and methyl orange by ZnO:Eu nanoparticles.* Applied Catalysis B: Environmental, 2017. **203**: p. 740-752.
11. Ma, J., et al., *Fenton Degradation of Organic Pollutants in the Presence of Low-Molecular-Weight Organic Acids: Cooperative Effect of Quinone and Visible Light.* Environmental Science & Technology, 2006. **40**(2): p. 618-624.
12. Holland, S.K., et al., *Photoelectrochemical performance of W-doped BiVO4 thin films deposited by spray pyrolysis*. Vol. 4. 2014: SPIE. 1-13, 13.
13. Pookmanee, P., et al., *Preparation and Characterization of BiVO4 Powder by the Sol-gel Method.* Ferroelectrics, 2013. **456**(1): p. 45-54.
14. Regmi, C., D. Dhakal, and S.W. Lee, *Visible-light-induced Ag/BiVO4 semiconductor with enhanced photocatalytic and antibacterial performance.* Nanotechnology, 2018. **29**(6): p. 064001.
15. Tang, Z.-R., Q. Yu, and Y.-J. Xu, *Toward improving the photocatalytic activity of BiVO4–graphene 2D–2D composites under visible light by the addition of mediator.* RSC Advances, 2014. **4**(102): p. 58448-58452.
16. Zhang, L., et al., *Mechanochemically synthesized CuO/m-BiVO4 composite with enhanced photoelectrochemical and photocatalytic properties.* RSC Advances, 2016. **6**(69): p. 65038-65046.
17. Basavalingaiah, K.R., et al., *Uniform deposition of silver dots on sheet like BiVO4 nanomaterials for efficient visible light active photocatalyst towards methylene blue degradation.* FlatChem, 2020. **19**: p. 100142.
18. Wang, P., et al., *Selective construction of junctions on different facets of BiVO4 for enhancing photo-activity.* New Journal of Chemistry, 2015. **39**(12): p. 9918-9925.
19. Liqiang, J., et al., *Review of photoluminescence performance of nano-sized semiconductor materials and its relationships with photocatalytic activity.* Solar Energy Materials and Solar Cells, 2006. **90**(12): p. 1773-1787.
20. Thomas, S., et al., *Oxidative degradation of Acid Red 1 in aqueous medium.* Chemical Engineering Journal, 2014. **244**: p. 473-482.
21. Ildefonso, Z.T., et al., *A phenomenon of degradation of methyl orange observed during the reaction of NH4TiOF3 nanotubes with the aqueous medium to produce TiO2 anatase nanoparticles.* RSC Advances, 2016. **6**(80): p. 76167-76173.
22. Nguyen, C.H., C.-C. Fu, and R.-S. Juang, *Degradation of methylene blue and methyl orange by palladium-doped TiO2 photocatalysis for water reuse: Efficiency and degradation pathways.* Journal of Cleaner Production, 2018. **202**: p. 413-427.
23. Rauf, M.A., et al., *Photocatalytic degradation of Methylene Blue using a mixed catalyst and product analysis by LC/MS.* Chemical Engineering Journal, 2010. **157**(2): p. 373-378.
24. Saha, S., J.M. Wang, and A. Pal, *Nano silver impregnation on commercial TiO2 and a comparative photocatalytic account to degrade malachite green.* Separation and Purification Technology, 2012. **89**: p. 147-159.

25. Thao, N.T., et al., *Advanced oxidation of rhodamine B with hydrogen peroxide over ZnCr layered double hydroxide catalysts.* Journal of Science: Advanced Materials and Devices, 2017. **2**(3): p. 317-325.
26. Pingmuang, K., et al., *Composite Photocatalysts Containing BiVO(4) for Degradation of Cationic Dyes.* Scientific reports, 2017. **7**(1): p. 8929-8929.
27. Rochkind, M., S. Pasternak, and Y. Paz, *Using Dyes for Evaluating Photocatalytic Properties: A Critical Review*. Vol. 20. 2014. 88-110.
28. Chen, L., et al., *Controllable synthesis of hollow and porous Ag/BiVO4 composites with enhanced visible-light photocatalytic performance.* RSC Advances, 2013. **3**(46): p. 24354-24361.
29. Fan, H., et al., *The preparation of high photocatalytic activity nano-spindly Ag-BiVO4 and photoinduced carriers transfer properties.* Chemical Physics Letters, 2015. **640**: p. 188-193.
30. Huang, C.-K., et al., *Enhanced photocatalytic performance of BiVO4 in aqueous AgNO3 solution under visible light irradiation.* Applied Surface Science, 2017. **399**: p. 10-19.
31. Xu, X., et al., *New insights into Ag-doped BiVO4 microspheres as visible light photocatalysts.* RSC Advances, 2016. **6**(101): p. 98788-98796.